



Andrew, J. J., Schneider, J., Schiffer, A., Hafeez, F. and Kumar, S. (2022) Dynamic crushing of tailored honeycombs realized via additive manufacturing. *International Journal of Mechanical Sciences*, 219, 107126. (doi: [10.1016/j.ijmecsci.2022.107126](https://doi.org/10.1016/j.ijmecsci.2022.107126))

The material cannot be used for any other purpose without further permission of the publisher and is for private use only.

There may be differences between this version and the published version. You are advised to consult the publisher's version if you wish to cite from it.

<https://eprints.gla.ac.uk/264603/>

Deposited on 02 February 2022

Enlighten – Research publications by members of the University of  
Glasgow

<http://eprints.gla.ac.uk>

# Dynamic crushing of tailored honeycombs realized via additive manufacturing

Jefferson Andrew J<sup>a</sup>, Johannes Schneider<sup>b</sup>, Andreas Schiffer<sup>a</sup>, Farrukh Hafeez<sup>c</sup>, S Kumar<sup>b,d\*</sup>

<sup>a</sup> Department of Mechanical Engineering, Khalifa University of Science and Technology, Abu Dhabi, 127788, UAE

<sup>b</sup> James Watt School of Engineering, University of Glasgow, Glasgow G12 8QQ, UK

<sup>c</sup> Department of Mechanical Engineering, University of Birmingham-Dubai, Dubai, UAE.

<sup>d</sup> Glasgow Computational Engineering Centre, University of Glasgow, Glasgow G12 8LT, UK

## Abstract

Enhancing the energy absorption characteristics of a material/structure without compromising its strength and stiffness has been a long-standing challenge in the pursuit of lightweight engineering. Here, we introduce a novel tailoring strategy where the wall thickness of the honeycombs is bi-linearly graded along the out-of-plane direction to tune their energy absorption and impact resistance by varying two design parameters, the gradation parameter  $\alpha$  and the normalized taper length  $\eta'$ . Based on the proposed scheme, hexagonal honeycombs of the same mass and varying parameters  $[\alpha, \eta']$  were designed and realized via Digital Light Processing (DLP) additive manufacturing. Low-velocity out-of-plane impact tests and dynamic FE calculations were performed to examine the collapse response of geometrically tailored honeycombs and assess their energy absorption characteristics and collapse mechanisms in relation to those observed in conventional (non-tailored) honeycombs of the same mass. The measurements and predictions revealed that the bi-linearly wall-thickness tailored honeycombs consistently outperform their non-tailored counterparts when the impact energy is high, reporting an increase in energy absorption as high as 250%. Such remarkable enhancement in energy absorption is attributed to a transition in the underlying collapse mechanism from global buckling mode to progressive crushing of the cell-walls. We also examined the impact response of honeycombs with periodic variations in cell-wall thickness and found that the latter structures collapse rapidly in an unstable manner, similar to what observed in conventional honeycombs, leading to limited capacity to dissipate the impact energy. With careful selection of the design parameters  $[\alpha, \eta']$ , we demonstrate experimentally that bilinearly wall-thickness tailored honeycombs can exhibit simultaneous improvements in energy absorption and impact resistance, providing new opportunities for expanding the property space of honeycombs and opening the door for a wide range of applications.

---

\* Corresponding author: [s.kumar@eng.oxon.org](mailto:s.kumar@eng.oxon.org)

**Keywords:** Low-velocity impact; additive manufacturing; geometrically tailored honeycombs; mechanical metamaterials; dynamic FE simulation

## 1. Introduction

Honeycombs are extensively considered in lightweight engineering to create stiffer and stronger structures for a wide range of applications, particularly in the aerospace, automotive and defense industries [1-4]. When honeycombs are subject to impact or blast loading, their hollow structure collapses and, consequently, a significant amount of the kinetic energy is dissipated through inelastic deformation of the cell walls, resulting in effective shock mitigation [5]. The impact resistance and energy absorption characteristics of honeycombs are strongly affected by the properties of the constituent material and the unit-cell geometry [6-11]. Over the years, the energy absorption characteristics of honeycombs with different unit-cell geometries (e.g. square [12], triangular [13], Kagome [14], circular [15] and hexagonal sections [16] [17]) have been studied in the context of blast or impact protection [18]. Among various unit-cell geometries, research on hexagonal honeycombs, drawing inspiration from natural patterns, has advanced rapidly, owing to their ease of manufacture and their favorable mechanical characteristics [11].

Recent advances in manufacturing technologies have prompted active research in spatially tailored cellular structures [5-7, 19]. In honeycombs, spatial gradients can be realized in three different ways: (i) cell-wall thickness gradients [20-22], (ii) unit-cell size gradients [23, 24] or (iii) material gradients [25, 26]. For example, spatial variations in yield stress were studied in layered materials by Shen et al. [25, 26] and observed a double shock mode when negative gradients were employed. However, cellular structures with material gradients face manufacturing constraints, and therefore, the main body of the literature concerned with functionally graded honeycombs focuses on gradients in the relative density which allow the properties and functionalities of honeycomb structures to be optimally engineered to desired applications [7, 27, 28]. It is well-known that the conventional honeycombs are mostly composed of thin-walled structural ligaments with uniform thickness [29]. In real-life, the energy absorbing structural components experience very complex loadings with spatially varying non-uniform stresses, indicating that

different portions of the structure or component should possess different mechanical characteristics (for optimal deformation modes that mitigate undesirable failure modes) to optimally utilize the total material volume [5, 30-32]. Hence, a uniform cell-wall thickness does not make optimal use of the material to absorb impact energy [33, 34], and therefore it is crucial to develop new structural designs with appropriate thickness distribution for improving energy absorption properties and material utilization [35]. Additionally, such geometrically tailored designs of cell walls of honeycombs can mitigate undesirable failure or collapse modes [36]. Similarly, Ajdari et al. [21] investigated the in-plane impact response of honeycomb structures with gradual changes in cell-wall thickness, reporting enhanced energy absorption during the early collapse phase when the relative density was decreased in the direction of crushing. Other authors [22] [23] studied the damage mechanisms and energy absorption characteristics of Voronoi honeycombs with density gradients and reported that positive gradients could increase the absorbed energy while decreasing the peak contact force [23]. Honeycombs with variable wall thickness have also been studied more recently in [1], [5], [37], reporting an enhanced impact performance as compared to non-graded structures under various loading scenarios.

Useful guidelines for the design of functionally graded honeycombs can also be drawn from studies on axial crushing of functionally graded tubes [23]. For example, Zhang et al. [38] reported that a square tube with functionally graded thickness (FGT) along the lateral direction can result in an increase in specific energy absorption (SEA) of 30 – 35% in comparison with the non-tailored tubes. Further, Sun et al. [3] developed a square tube with FGT along the out-of-plane direction and noticed that the SEA of the graded tube is higher (15.20 %) than that of its non-tailored counterpart. The FGT approach is found to have a substantial effect on both the collapse mechanisms and energy absorption characteristics of the tubes [39, 40]. The crushing characteristics of circular tubes with FGT can be found in [5, 41]. A recent study showed enhanced crushing characteristics of a hybrid tube composed of a conventional circular tube surrounded by an auxetic outer tube in a co-axial manner [42].

Impact loads produce complex stress-strain responses in the honeycomb structures, depending on the nature of the load, such as low-velocity, high-velocity, and blast loading [43-46]. Given that the mutual interaction between damage modes is very complex at low velocities, damage mechanisms can be better understood by conducting real-time experiments at such velocities. Previous studies on honeycomb structures with spatially graded features were performed mostly via numerical and/or analytical approaches [18, 28, 47, 48], as the fabrication of complex cellular structures via traditional manufacturing techniques continued to be a challenge. Therefore, experimental studies on honeycombs under out-of-plane impact loading are mostly limited to simple topologies and uniform cell-wall thickness. However, recent advances in additive manufacturing (AM) technologies have facilitated the fabrication of structured materials with spatially tailored architecture and/or material properties at different length scales [49-51], thus providing new opportunities for expanding the property space of cellular materials and enhancing their functionalities [7, 52-57]. This was recently demonstrated by Kumar et al. [32], where AM was utilized to realize spatially tailored honeycombs with varying cell-wall thickness and shown that the energy absorption efficiency under out-of-plane compression can be as high as 90%, by far outperforming practical microarchitected metamaterials. Such remarkable increase in SEA was the result of a transition from sudden collapse by global buckling (associated with low SEA) to progressive failure by local buckling/wrinkling of the cell walls (associated with high SEA). Such tailoring scheme was also shown to be effective under low velocity impact where an increase in energy absorption of 60% was reported [7]. While previous studies have shown that wall-thickness gradients in honeycombs can substantially enhance their mass specific energy absorption, the aforementioned gradient design concepts often compromise the overall structural integrity and therefore result in reduced strength, stiffness and /or damage tolerance, particularly when loads of lower intensity are applied repeatedly [7]. Improving the toughness of honeycomb structures without sacrificing the overall stiffness and/or strength has been an abiding challenge, as these mechanical properties are usually mutually antagonistic [49, 58].

To overcome current limitations in the mechanical characteristics of honeycombs, we propose, in this paper, a novel design scheme that provides tunable strength and energy absorption through introduction of a bilinear gradient in the cell-wall thickness. We show that the proposed tailoring scheme makes it possible to simultaneously tune the impact resistance and energy absorption under out-of-plane compression by mitigating the global collapse mode of the honeycombs. Stereolithography-based AM is used to realize geometrically tailored hexagonal honeycombs from photocurable resin (PlasGRAY<sup>TM</sup>), and their dynamic responses and collapse mechanisms under out-of-plane compression were experimentally and numerically examined through low-velocity impact tests and explicit FE calculations, respectively. To examine the effects of impact mass and velocity on their dynamic collapse response, equi-energetic impact tests were performed on selected honeycomb designs at both low (15 J) and high levels (130 J) of impact energy. We also examined the effect of impact direction by inverting the gradation pattern in the honeycombs, and we explored the impact responses of honeycombs with periodic variations in the cell-wall thickness, obtained by stacking bilinear gradation patterns in a systematic way. The numerical and experimental results presented in this study provide adequate guidelines for the design and application of wall-thickness tailored honeycombs in high performance structural applications [12]. The outline of this paper is as follows: in Section 2, we describe the experimental techniques involved in the fabrication and mechanical testing of the honeycombs; in Section 3, we present and discuss the results obtained from the low-velocity impact tests and dynamic FE calculations and finally, in Section 4, we present the key findings of this study.

## **2. Experimental and numerical procedure**

This section presents the materials, design idea, and fabrication procedure employed to manufacture the honeycombs. The formulas used for configuring different geometries of tailored honeycomb samples with graded walls are given. The low-velocity impact set up for the experimental test is introduced, and the finite element (FE) modeling procedure is also presented.

### **2.1. Materials and fabrication**

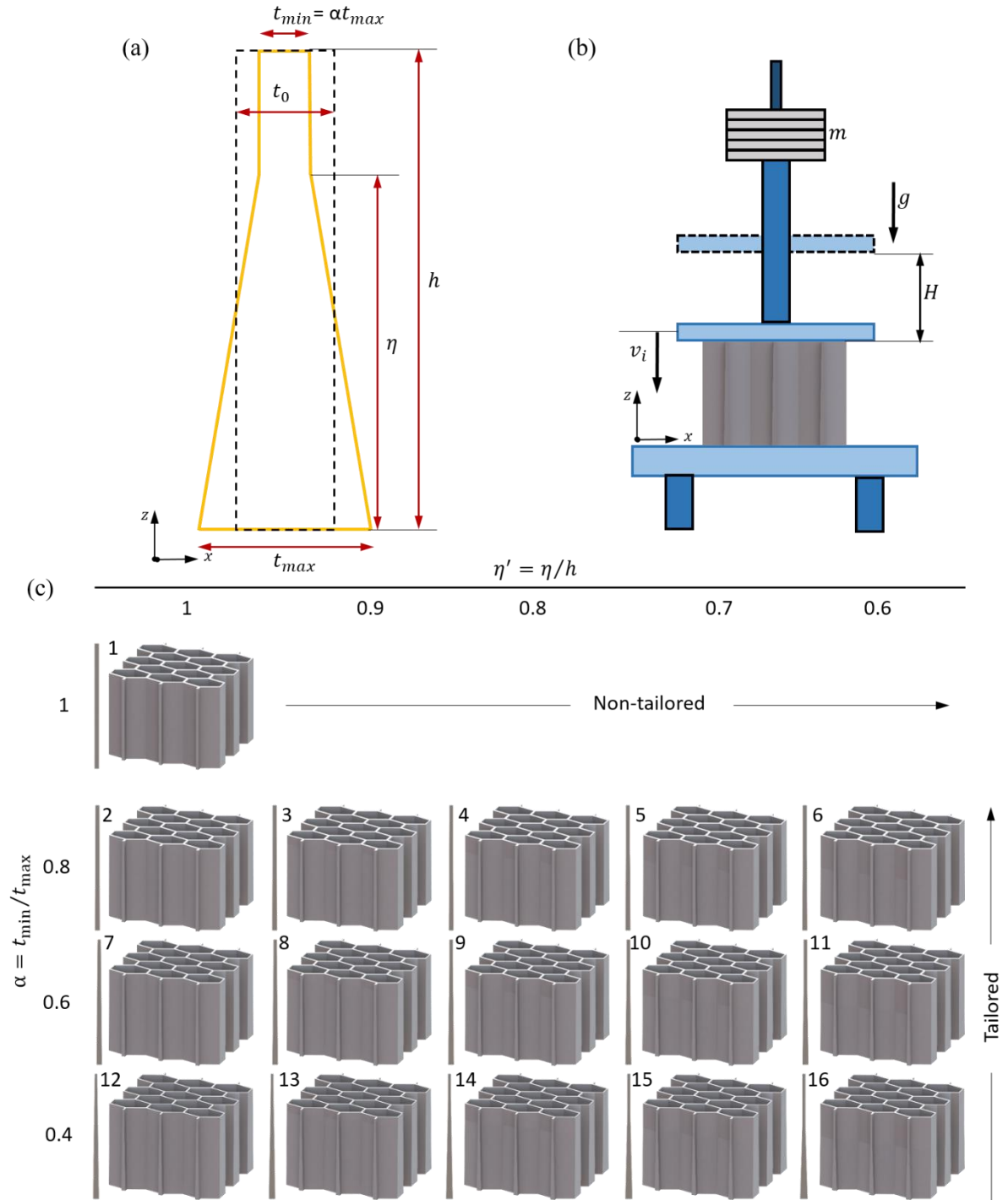


Figure 1: (a) Schematic showing the wall profile of bi-linearly graded honeycomb structures, (b) schematic of the drop weight impact setup, and (c) CAD images and corresponding wall profiles of (1) uniform thickness and (2-16) geometrically tailored honeycombs.

An Asiga PRO2 desktop 3D printer was employed to fabricate the honeycomb structures via slide and separate™ (SAS™) 3D printing technology. All honeycombs were fabricated using PlasGRAY™

photopolymer and were of relative density,  $\bar{\rho} = 19\%$ . Soon after 3D printing, all samples were post-cured by UV light for 120 s to increase the cross-link density in the printed samples. The process parameters for additive manufacturing are summarized in Table S1 (Supplementary Material), while the mechanical, thermal and physical properties of PlasGRAY™ are listed in Table S2. Asiga Composer™ software (version 1.2.9) was used to set the printing process parameters and generate the sliced file required for the SAS process. As shown in Fig. 1a, we consider geometrically tailored honeycombs with bilinear wall thickness gradients along the out-of-plane direction of the honeycomb, as well as conventional (non-tailored) honeycombs with uniform cell wall thickness  $t_0$ , and their geometrical parameters are listed in Table 1. The bilinear gradation pattern (see Fig. 1a) consists of a tapered base and a neck at the top with uniform cross-section, and its geometry can be described by two non-dimensional parameters, the (i) gradation parameter,  $\alpha = \pm t_{min}/t_{max}$ , where  $t_{min}$  and  $t_{max}$  represent the minimum and maximum wall thickness, respectively, and the (ii) normalized gradation length of the tapered base,  $\eta' = \eta/h$ , where  $\eta$  is the height of the tapered base and  $h$  is the total height of the honeycomb. Note that in the limit of  $\eta' \rightarrow 1$ , the bi-linear gradient becomes a linear gradient and in the limit of  $\alpha \rightarrow 1$ , the cell wall thickness becomes uniform (non-tailored case).

Table 1: Geometrical parameters of non-tailored and tailored honeycomb structures.

Case	h (mm)	$t_0$ (mm)	$\eta$	$\eta'$	$t_{min}$ (mm)	$t_{max}$ (mm)	$\alpha$
1	30	1	30	1	1	1	1
2	30	1	30	1	0.89	1.11	0.8
3	30	1	27	0.9	0.90	1.12	0.8
4	30	1	24	0.8	0.91	1.14	0.8
5	30	1	21	0.7	0.92	1.15	0.8
6	30	1	18	0.6	0.93	1.16	0.8
7	30	1	30	1	0.75	1.25	0.6
8	30	1	27	0.9	0.77	1.28	0.6
9	30	1	24	0.8	0.79	1.32	0.6
10	30	1	21	0.7	0.81	1.35	0.6
11	30	1	18	0.6	0.83	1.39	0.6

12	30	1	30	1	0.57	1.43	0.4
13	30	1	27	0.9	0.60	1.49	0.4
14	30	1	24	0.8	0.63	1.56	0.4
15	30	1	21	0.7	0.66	1.64	0.4
16	30	1	18	0.6	0.69	1.72	0.4

We also note that the sign of the gradation parameter  $\alpha$  is taken as positive (+) in case the wall thickness in the graded portion increases in impact direction, while  $\alpha$  is considered negative (-) if the cell wall thickness decreases in the direction of impact. Fig. 1c shows a map of the generated honeycomb geometries with their respective cell wall profiles, noting that the overall in plane dimensions (41.4 mm  $\times$  41.4 mm), height  $h = 30$  mm and the number of unit cells (3  $\times$  3) were kept constant in all samples.

## 2.2. Low-velocity impact tests

Low-velocity drop weight impact tests were performed according to ASTM D7136 standard by employing a CEAST 9350 impact tower with a 30 kN dynamic load cell. The velocity of the drop mass was measured by an optical laser measurement system. The load cell was connected to a data acquisition system (CEAST DAS 64k) with a sampling rate of 3 MSPS (Million Samples per Second). As shown in Fig. 1b, the samples were placed on the flat base of the machine and a flat-ended cylindrical steel block of 60 mm diameter was dropped from a given height  $H$  to subject the sample to uniform out-of-plane compression during the test. The impact energy was adjusted by varying the mass  $m$  and/or drop height  $H$  of the impactor. To prevent repeated impacts on the same sample in a single test, an automatic braking system was used to arrest the motion of the rebounding striker. Two types of loading protocols were used: (1) impact loading performed with the same drop mass  $m = 16.75$  kg and velocity  $v_i = 3.86$  m/s resulting in an impact energy of 130 J, and (2) equi-energetic impacts with 15 J and 125 J, realized with various combinations of  $m$  and  $v_i$ . The parameters used for the equi-energetic impact tests are summarized in Table 2.

Table 2: Summary of test parameters for equi-energetic impacts performed with 15 J and 125 J.

Impact Energy (J)	Impact mass, $m$ (kg)	Average Impact Velocity, $v_i$ (m/s)	Drop Height, $H$ (mm)	Momentum (kg m/s)
15 J	11.75	1.60	130	18.80
	16.75	1.34	91	22.45
	21.75	1.17	70	25.45
	26.75	1.06	57	28.36
125 J	11.75	4.61	1085	54.17
	16.75	3.86	761	64.66
	21.75	3.39	586	73.73
	26.75	3.06	476.5	81.86

The time histories of striker displacement  $\delta(t)$  and velocity  $v(t)$  were determined by evaluating

$$\delta(t) = \delta_i + v_i t + \frac{gt^2}{2} - \int_0^t \left( \int_0^t \frac{F(t)}{m} dt \right) dt \quad (1)$$

and

$$v(t) = v_i + gt - \int_0^t \frac{F(t)}{m} dt \quad , \quad (2)$$

respectively, where  $\delta_i$  is the striker displacement at time  $t = 0$  (incipient contact with the target),  $v_i$  is the striker velocity at time  $t = 0$  (measured by the optical laser system),  $m$  is the total striker mass,  $g$  is the gravitational acceleration and  $F(t)$  is the contact force at time  $t$  (measured by the load cell). Then, the energy absorbed by the sample at time  $t$  can be calculated using

$$E_a(t) = \frac{m(v_i^2 - (v(t))^2)}{2} + mg\delta(t) \quad . \quad (3)$$

### 2.3. Finite element modelling

Dynamic FE calculations were performed in ABAQUS/Explicit to simulate the collapse response of the architected honeycombs considered in this study. A shell model of the entire honeycomb structure ( $41.4 \times 41.4 \times 30$  mm) was developed in ABAQUS and meshed using four-node shell elements with reduced integration (S4R in ABAQUS), finite membrane strains and seven integration points through the thickness of the element. The element size was set globally to  $l_e = 0.4$  mm, giving 65,475 elements in total, as shown in Fig. S1 (Supplementary Material). Note that further reductions in the mesh size caused the

computation time to increase substantially without significantly changing the predicted collapse response. The wall thickness gradient of the honeycomb was implemented in the model by adjusting the element thickness,  $t_e$ , in accordance with

$$t_e(z) = \left[ t_{max} - (t_{max} - t_{min}) \frac{z}{\eta} \right] \left| \text{floor} \left( \frac{z}{\eta} - 1 \right) \right| + t_{min} \text{floor} \left( \frac{z}{\eta} \right) \quad (4)$$

where  $z$  represents the coordinate parallel to the through-thickness direction of the honeycomb, with  $z = 0$  at the base. The FE calculations were performed on non-tailored ( $\alpha = 1.0$ ,  $\eta' = 1.0$ ) and tailored honeycombs with  $\alpha = \{0.4, 0.6, 0.8\}$  and  $\eta' = \{0.6, 0.8, 1.0\}$ , giving a total of 10 different structures. The base of the drop weight tower and the flat-ended impactor were represented in the model by rigid surfaces, and these were placed in contact with the bottom and top face of the honeycomb, respectively. The inertia of the drop weight was accounted for by assigning a point mass in the range of 11.8 – 26.7 kg to the top surface through a reference point. The contact interactions between the honeycomb and the rigid surfaces as well as the self-contact between the collapsing cell walls were modelled using the “General Contact” capability in ABAQUS/Explicit with a friction coefficient of 0.2 against tangential sliding. The bottom surface was kept fully fixed during the analysis, while the top surface was imposed an initial velocity  $v_0$  in the  $z$ -direction in the range of 3.1 – 4.6 m s<sup>-1</sup>, to mimic various impact conditions in line with our experiments. Note that the top surface was only allowed to move freely in the  $z$ -direction and had all other DOFs fully constrained.

The elastic response of the PlasGRAY<sup>TM</sup> resin (density  $\rho_s = 1180 \text{ kg m}^{-3}$ ) was modeled using isotropic linear elasticity with Young’s modulus  $E_s = 950 \text{ MPa}$  and Poisson’s ratio  $\nu_s = 0.4$  (in line with our experiments, see Fig. S2, Supplementary Material), while the inelastic response of the resin was described using the Drucker-Prager (DP) plasticity model [59]. The friction angle in the DP model was chosen as  $\beta = 37^\circ$  to match the pressure-sensitive yielding of the polymer, as observed from uniaxial tension and compression experiments performed in this study (see Fig. S2, Supplementary Material). To limit the dilation of the polymer during plastic straining, we chose a non-associated flow rule with the dilation angle set close to

zero [32], while the eccentricity parameter in the flow potential was set to  $\epsilon = 0.1$  [32]. Strain hardening in compression was modelled based on the uniaxial stress vs. strain data plotted in Fig. S2b (Supplementary Material), while the strain rate dependence of the flow stress was assumed to follow the Eyring model [60].

$$\dot{\gamma}_p = \dot{\gamma}_0 \exp\left(\frac{\tau_{eq}}{\tau_0}\right) \quad \text{where} \quad \tau_0 = \frac{RT}{V_0}. \quad (4)$$

Here,  $\dot{\gamma}_p$  is the plastic shear strain rate,  $\tau_{eq}$  is the applied equivalent shear stress,  $\dot{\gamma}_0$  is a pre-exponential factor,  $R$  is the gas constant,  $T$  is the temperature,  $V_0$  is the activation volume and  $\tau_0$  is a reference stress describing the degree of rate sensitivity. Note that under uniaxial loading,  $\tau_{eq} = \sigma/\sqrt{3}$  and  $\dot{\gamma}_p = \sqrt{3}\dot{\epsilon}$ , where  $\sigma$  and  $\dot{\epsilon}$  are the applied stress and strain rate, respectively. Under isothermal conditions, the rate sensitivity  $\tau_0$  is a constant and can be determined by fitting eq. (4) to yield stress vs. strain rate data. However, for the PlasGRAY<sup>TM</sup> resin used in this study, stress vs. strain curves have so far only been reported for quasi-static strain rates, and therefore, we performed a least-square fit of eq. (4) to the yield stress vs. strain rate data reported in [61] for a similar DGEBA based photocurable resin where the yield strength of the photo-resin increased by ~65% between strain rates of 0.001 and 1 s<sup>-1</sup>, yielding  $\tau_0 = 2.49$  MPa. The obtained rate sensitivity was then used in the Eyring model (eq. (4)) to generate a family of stress vs. strain curves based on the measured quasi-static compressive response of the PlasGRAY<sup>TM</sup> resin (Fig. S2b, Supplementary Material) and these were then used to define the rate-dependent strain hardening behavior in ABAQUS. Damage initiation and evolution was also included in the constitutive description by using the ‘‘Ductile Damage Model’’ in ABAQUS, which is based on concepts of continuum damage mechanics. In this model, the equivalent plastic strain (i.e. power conjugate to the von Mises stress) at the initiation of damage,  $\epsilon_i^p$ , was specified for different values of stress triaxiality  $T$ , to account for the pressure-sensitive failure strain of the PlasGRAY<sup>TM</sup> resin, as observed from our uniaxial tension/compression experiments (Fig. S2). Since thermoset polymers typically fail at lower strains under elevated deformation rates [62], the plastic failure strains ( $\epsilon_i^p = 0.15$  at  $T = -0.3$  and  $\epsilon_i^p = 0.03$  at  $T = 0.3$ ) in the model were chosen lower than those measured under quasi-static conditions, which resulted in brittle

crushing of the cell walls, as observed in our impact experiments. Following the initiation of damage, the material stiffness was gradually degraded using an energy-based linear damage evolution law with the fracture energy set to  $G_f = 10 \text{ N m}^{-2}$ . We note that the effect of  $G_f$  on the collapse response of the honeycomb was relatively small over the range  $1 \text{ N m}^{-2} \leq G_f \leq 100 \text{ N m}^{-2}$ , according to our preliminary FE calculations. To replicate numerically the buckling of the cell walls during the impact response, as observed experimentally, we initially performed a buckling analysis in ABAQUS for each type of honeycomb structure using the same geometry, mesh and boundary conditions as described above. The shape of the first buckling mode was extracted from the latter analysis and was then used as a geometric imperfection in the dynamic FE calculations, where a small perturbation amplitude of  $t_0/100$  was sufficient to trigger elastic buckling in the FE analysis. The analysis was performed up to the point of full densification (or until the impactor rebounded), and the time histories of the displacement and contact force applied on the loading surface (on top of the sample) were extracted from the FE analysis outputs.

### 3. Results and discussion

In this section, experimental and finite element (FE) results of the dynamic collapse behavior of graded honeycombs, including the effect of various design parameters and strain rates are discussed. Besides, the impact response of honeycombs with periodic thickness variations in the out-of-plane direction is also presented.

#### 3.1. Effect of the design parameters $\alpha$ and $\eta'$

In this section, we investigate the effects of the gradation parameter  $\alpha$  and normalized gradation length  $\eta'$  on the impact responses of the 3D printed honeycombs. Figs. 2a, c and e show the contact force vs. displacement curves of graded honeycombs with  $\alpha = 0.8, 0.6$  and  $0.4$ , respectively, measured at an impact energy of 130 J, while the corresponding energy vs. time histories are illustrated in Figs. 2b, d and f, respectively. In each of these figures, contours are included for five different choices of normalized gradation length,  $\eta' = \{1, 0.9, 0.8, 0.7, 0.6\}$ , along with the measurements obtained for the non-tailored

counterpart. It can be seen that, for the case  $\alpha = 0.8$ , the contact force vs. displacement (Fig. 2a) and energy vs. time traces (Fig. 2b) for honeycombs with  $\eta' = \{0.6, 0.7, 0.8, 0.9\}$  are very similar and follow the trends observed for the non-tailored sample. As shown in Fig. 2a, the contact force on the samples (excluding  $\eta' = 1.0$ ) reaches a peak at a deformation of only  $\sim 2$  mm and quickly vanishes thereafter, suggesting that these samples underwent sudden collapse by unstable propagation of cracks in the honeycomb walls. The geometrically tailored honeycombs only have a clear advantage over their non-tailored counterpart for the case of  $\eta' = 1$  (i.e. tapered wall along entire height of the honeycomb with a linear gradient) where the sample responds to the impact with a fluctuating contact force following the initial peak (see Fig. 2a), enabling a relatively stable collapse response and resulting in a significant increase in energy absorption (see Fig. 2b). It has been shown previously [7] that the energy absorption of graded honeycombs increases with increasing thickness gradient, and this is also observed in the present work where samples with  $\alpha = 0.6$  (see Fig. 2c) and  $\alpha = 0.4$  (see Fig. 2e) offer a persistent, albeit fluctuating, resistance against structural collapse for all choices of  $\eta'$  considered here, and therefore absorb kinetic energy more effectively as compared to their non-tailored counterparts (see Figs. 2d and f).

In Fig. 3, we compare the measured contact force vs. displacement histories of non-tailored (Fig. 3a) and tailored (Figs. 3b-d) honeycombs to those obtained from the dynamic FE calculations. The FE model is able to capture the sudden and unstable collapse of the non-tailored ( $\alpha = 1.0$  and  $\eta' = 1.0$ ) and tailored honeycomb with  $\alpha = 0.8$  and  $\eta' = 0.8$ , as seen from Figs. 3a and b, respectively. For the honeycombs with smaller  $\alpha$  values (see Figs. 3c-d), the model predicts fluctuating contact forces following the initial peak, and this is also found in good qualitative agreement with the measured responses. However, the predictions of the initial peak load and the subsequent fluctuation amplitudes are somewhat under-predicted by the FE model. Two possible reasons for these discrepancies are: (i) geometric inaccuracies and/or material defects in the 3D printed structures (not accounted for in the FE calculations); and (ii) differences between the actual strain rate sensitivity of the PlasGRAY<sup>TM</sup> resin and the literature data that was used to describe the rate dependent hardening behavior in the DP model, as detailed in Section 3.

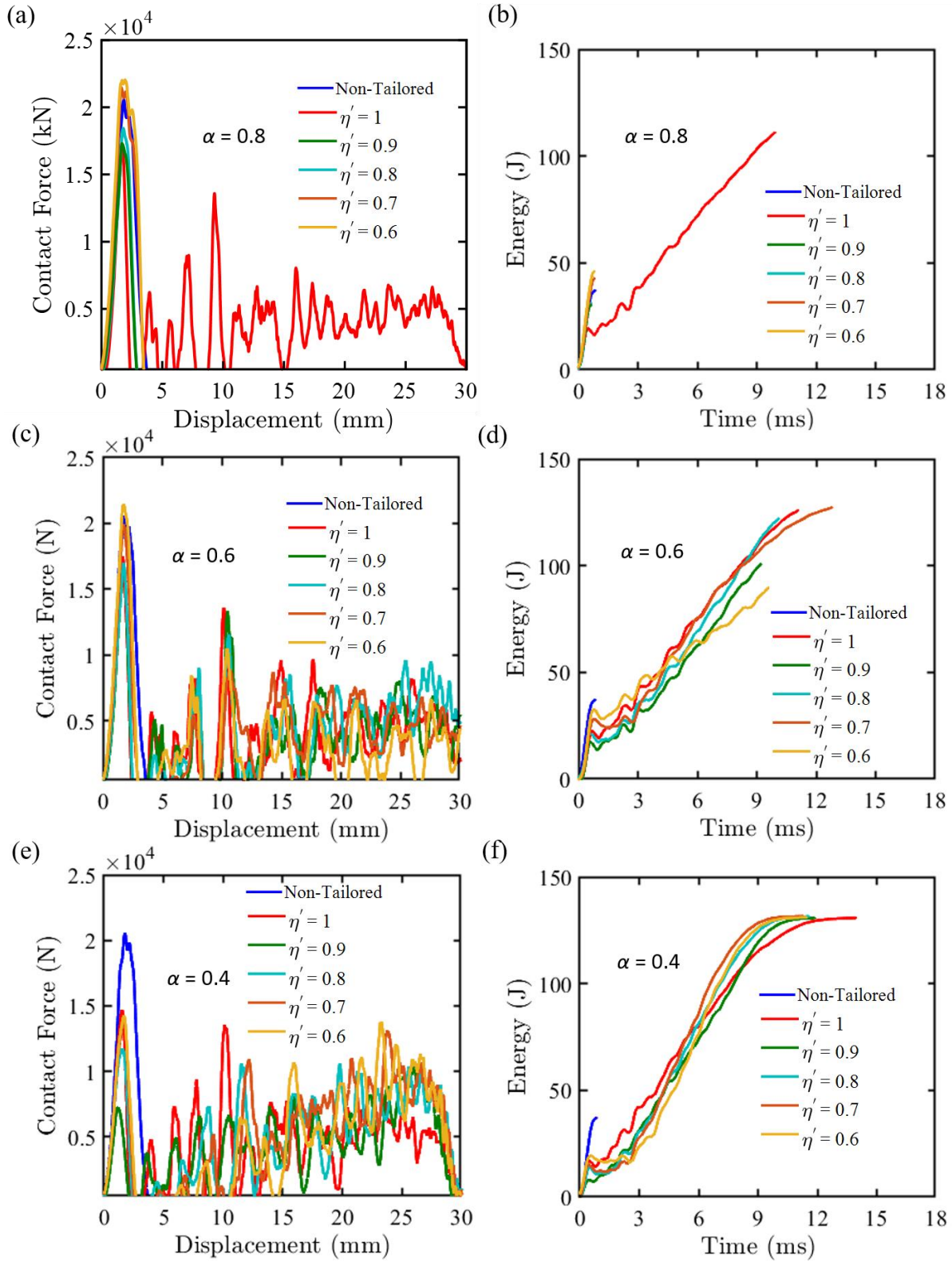


Figure 2: Low-velocity impact response of geometrically tailored honeycomb structures subject to an impact energy of 130 J: (a, c, e) contact force vs. displacement curves for different choices of gradation

parameter  $\alpha = \{0.8, 0.6, 0.4\}$ ; (b, d, f) time histories of absorbed energy for  $\alpha = \{0.8, 0.6, 0.4\}$ ; in all figures, contours are included for different choices of  $\eta' = \{1.0, 0.9, 0.8, 0.7, 0.6\}$ .

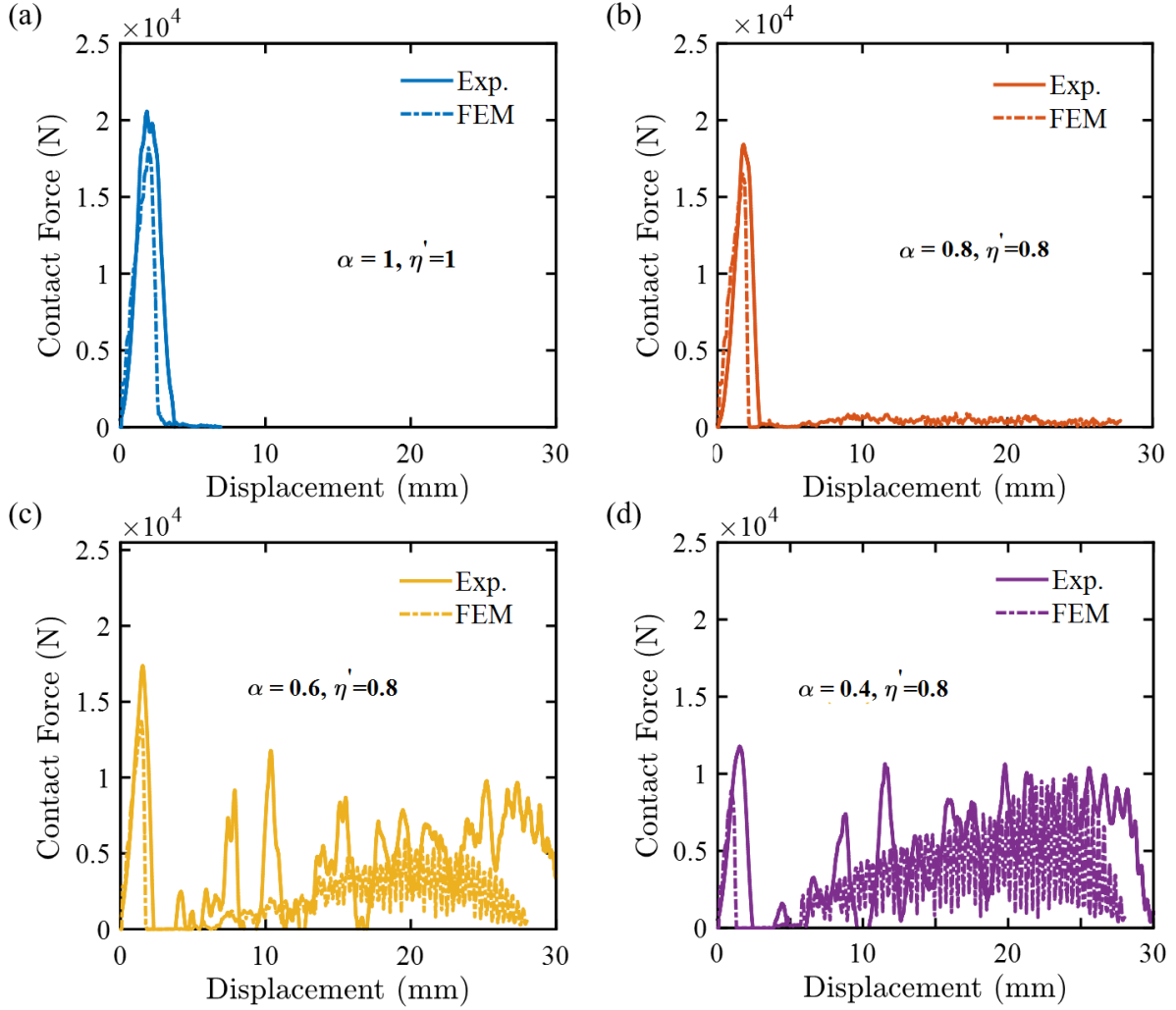


Figure 3: Predicted and measured contact force vs. displacement histories for: (a) non-tailored, (b) tailored honeycomb with  $\alpha = 0.8$  and  $\eta' = 0.8$ , (c) tailored honeycomb with  $\alpha = 0.6$  and  $\eta' = 0.8$ , and (d) tailored honeycomb with  $\alpha = 0.4$  and  $\eta' = 0.8$ .

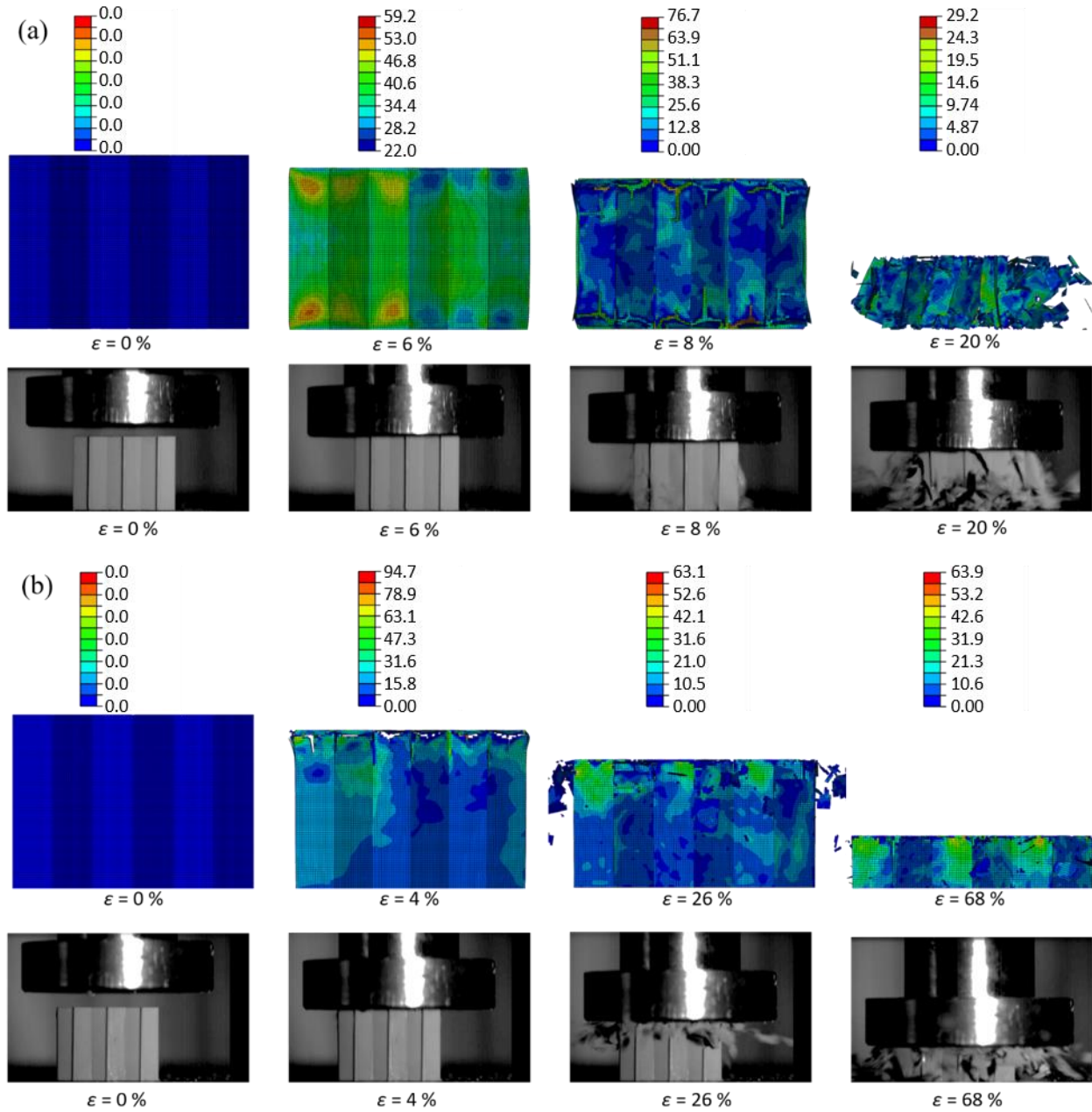


Figure 4: Illustration of the collapse response of (a) non-tailored and (b) tailored ( $\alpha = 0.4$  and  $\eta' = 1.0$ ) honeycombs; FE deformation maps (showing the von Mises stress in MPa) are compared to high-speed images recorded during the impact tests.

The relatively stable collapse response and enhanced energy absorption characteristics of tailored honeycombs can be explained with the help of Fig. 4 where high speed images and FE contour plots (von Mises stress in units of MPa) are presented to illustrate the impact response of a non-tailored ( $\alpha = 1.0$ ,  $\eta' = 1.0$ , see Fig. 4a) and tailored honeycomb ( $\alpha = 0.4$ ,  $\eta' = 1.0$ , see Fig. 4b). It can be seen from these images

in Fig. 4a that the non-tailored structure starts to collapse at a compressive strain of  $\varepsilon = 8\%$ , which coincides with the peak load in Fig. 3a, and fails in a brittle manner by fragmentation and splitting of cell walls. In contrast, the tailored honeycomb starts to fracture near the top face where the cell walls are thinner, and proceeds to collapse in a progressive manner by local wrinkling and crushing until the entire structure is reduced to small pieces of fragments. Such progressive failure mode is favorable in energy absorbing cellular structures, such as honeycombs, because it provides a sustained resistance against structural collapse, which elevates their total energy absorption capacity, as seen from Fig. 2. It is also worth noting that the predicted deformation maps in Fig. 4 are found in very good agreement with the experimental evidence, which suggests that the observed failure modes are adequately captured in our FE analyses.

Based on the data plotted in Fig. 2, we evaluated, for each choice of  $\alpha$ , the normalized peak contact force and normalized absorbed energy defined as

$$\bar{F} = \frac{F_{tailored}}{F_{non-tailored}} \quad \text{and} \quad \bar{E}_a = \frac{E_{a,tailored}}{E_{a,non-tailored}}, \quad (5)$$

respectively, and plotted the obtained data as functions of  $\eta'$  in Figs. 5a and b, respectively; we also included in these figures the corresponding FE predictions (dashed lines) as evaluated from eq. (5). The experimental data in Fig. 5a shows that honeycombs with lower values of  $\alpha$  possess lower initial peak loads due to the simultaneous decrease in the neck thickness  $t_{min}$  (see Table 1) which limits the collapse load of the structure, and this trend is reflected in the numerical predictions. Except for a few cases, the normalized peak force induced in the graded honeycombs during the impact increases with decreasing  $\eta'$  due to the concomitant increase in  $t_{min}$  (see Table 1), offering higher resistance against elastic buckling of the cell walls. The experimental data further shows that the graded honeycombs with  $\eta' \leq 0.65$  and  $\alpha \geq 0.6$  achieve  $\bar{F} > 1$ , indicating that their peak load is higher than that of the non-tailored counterpart. However, this finding could not be confirmed by our FE calculations which predict  $\bar{F} < 1$  for all tailored honeycomb structures in Fig. 5a. This discrepancy could be attributed to defects present in the 3D printed structure and geometric inaccuracies associated with printed structures, both of which were not considered in our FE

models. Although the neck thickness  $t_{min}$  of the graded honeycombs is always smaller than the wall thickness of the non-tailored honeycomb in a mass preserving tailoring scheme (see Table 1), the presence of the tapered base in the graded honeycomb reduces the height with constant thickness (i.e.  $h - \eta$ ), and this, in turn, leads to an increase in the resistance against buckling which might have outweighed the effect of the smaller wall thickness  $t_{min}$  in the experiments, for some choices of  $\alpha$  and  $\eta'$ . Post-test photographs of the collapsed honeycomb structures are presented in Fig. S3 (Supplementary Material), showing that the tapered base of some of the tailored honeycombs remained partially intact following the impact, and this was more evident for samples with larger thickness gradients (i.e. smaller values of  $\alpha$ ). Although a decrease of the parameter  $\alpha$  resulted in a reduction of the peak load at the onset of structural collapse (recall Fig. 5a), it also led to a gradual improvement in the energy absorption capacity of the graded honeycombs, as seen from Fig. 5b. This can be explained by the occurrence of progressive damage and failure in the tailored honeycombs (see Fig. 4), which enables the structure to sustain a high level of impact force over a prolonged period, resulting in a steady increase in energy absorption over time (see Fig. 2). While the non-tailored structures possess higher energy absorption in their initial peak load (see Figs. 2b, d, f), the “fluctuating plateau” (due to progressive failure) is missing in their collapse response (see Fig. 2a, c, e) and therefore they absorb less energy in total. Substantial improvements in energy absorption are observed for the samples with  $\alpha \leq 0.6$ , where the total energy absorption is about 250 % higher (experimentally) as compared to that measured for the non-tailored honeycomb of equal mass. For  $\alpha = 0.8$ , the absorbed energy drops sharply as the value of  $\eta'$  decreases from 1.0 to 0.8, due to the concomitant transition in failure mode from stable to sudden collapse of the honeycomb structure (see Fig. 2a); however, such transition in failure mode was not observed in the corresponding FE calculations which predicted a normalized absorbed energy  $\bar{E}_a \approx 1$ . Although the FE predictions capture the overall trends of the measurements in Fig. 5b, the measured  $\bar{E}_a$  values are more sensitive to variations in  $\eta'$  than the corresponding FE predictions. This difference might have been triggered by small geometric inaccuracies and defects produced by the 3D

printing process (not accounted for in the FE calculations), which can affect the deformation and failure characteristics of the structure.

In summary, our experimental results in Fig. 5 show that it is practically possible to achieve simultaneous improvements in strength and energy absorption by adopting geometrically tailored designs of honeycombs with  $\eta' \leq 0.7$  and  $\alpha \geq 0.6$ . However, when enhanced energy absorption is the prime objective of the design, honeycombs with steep gradients in the cell wall thickness (for e.g.,  $\alpha = 0.4$ ) offer the advantage of achieving optimal energy absorption while the strength of the honeycomb can be independently tuned by adjusting the parameter  $\eta'$ . In the following section, we further explore the impact response of graded honeycombs with fixed design parameters  $\alpha = 0.4$  and  $\eta' = 0.7$ ; specifically, we examine the effects of impact mass and velocity on their contact force and energy absorption characteristics.

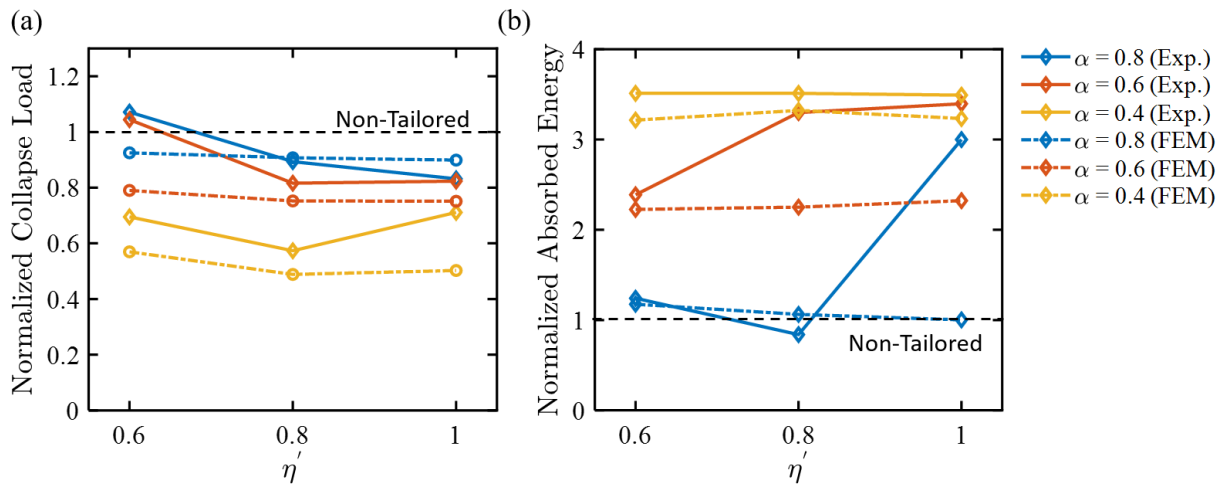


Figure 5: Predicted and measured low-velocity impact responses of geometrically tailored honeycomb structures subject to an impact energy of 130 J: (a) normalized peak force and (b) normalized absorbed energy as functions of the normalized taper length  $\eta'$  for different choices of gradation parameter  $\alpha = \{0.8, 0.6, 0.4\}$ .

### 3.2. Effect of impact mass and velocity

In this section, we examine the effect of strain rate on the dynamic collapse of graded honeycombs with  $\alpha = 0.4$  and  $\eta' = 0.7$  at low and high values of impact energy, 15 J and 125 J, respectively. To begin with, we present, in Figs. 6, contact force vs. displacement profiles obtained from equi-energetic impacts

at 15 J, performed with various combinations of impact mass and velocity. Note that the corresponding energy vs. time histories are presented in Fig. S4 (Supplementary Material). For the non-tailored samples, the contact force vs. displacement curves show evidence of elastic rebound of the striker (see Figs. 6a-d) which resulted in a drop in the energy vs. time histories (see Figs. S4) as the elastic strain energy stored in the sample was returned to the striker in the form of kinetic energy. Thus, the non-tailored samples absorbed only a part of the applied impact energy, and only their final energy values in Fig. S4 (rather than the peak values) were considered in the following comparison (see Fig. 7). These observations suggest that the impact load was not sufficient to induce significant damage in the non-tailored samples, and this is also evident from the post-test photographs shown in Fig. S5 (Supplementary Material). In contrast, no signs of elastic rebound were observed for the graded honeycombs in Figs. 6, suggesting that the latter samples underwent inelastic deformation and/or fracture during the impact. This can also be seen from the post-test photographs (see Fig. S5, Supplementary Material) showing fracture of the cell walls in the neck of the graded honeycomb (i.e. near top face) while the wider base remained nearly intact.

Based on the measurements presented in Figs. 6 and S4 (Supplementary Material), we determined the peak contact force, residual displacement, absorbed energy and contact duration for all equi-energetic loading conditions and plotted the obtained data in Fig. 7 as functions of the impact velocity. Note that the numerical values plotted in Fig. 7 are listed in Table S3 (Supplementary Material), for reference. At a low value of impact energy (15 J), the non-tailored samples show superior impact performance evinced by their higher peak contact force (Fig. 7a), lower residual displacement (Fig. 7b), longer contact duration (Fig. 7d) and higher damage resistance (Fig. S5, Supplementary Material) as compared to their tailored counterparts. For the non-tailored samples, decreasing the velocity (or increasing the striker mass) increases the peak contact force and contact duration besides reducing the residual deformation and absorbed energy. The tailored honeycombs show similar trends, except for Fig. 7a where the peak contact force slightly increases with increasing impact velocity. We argue that this small difference is due to the pronounced strain-rate dependence in the inelastic response of the 3D printed photo-resin used here (see section 3 for more details),

which would have more strongly affected the impact response of the tailored honeycombs since they showed a higher degree of damage (see Fig. S5, Supplementary Material) and inelastic deformation (see Fig. 7b).

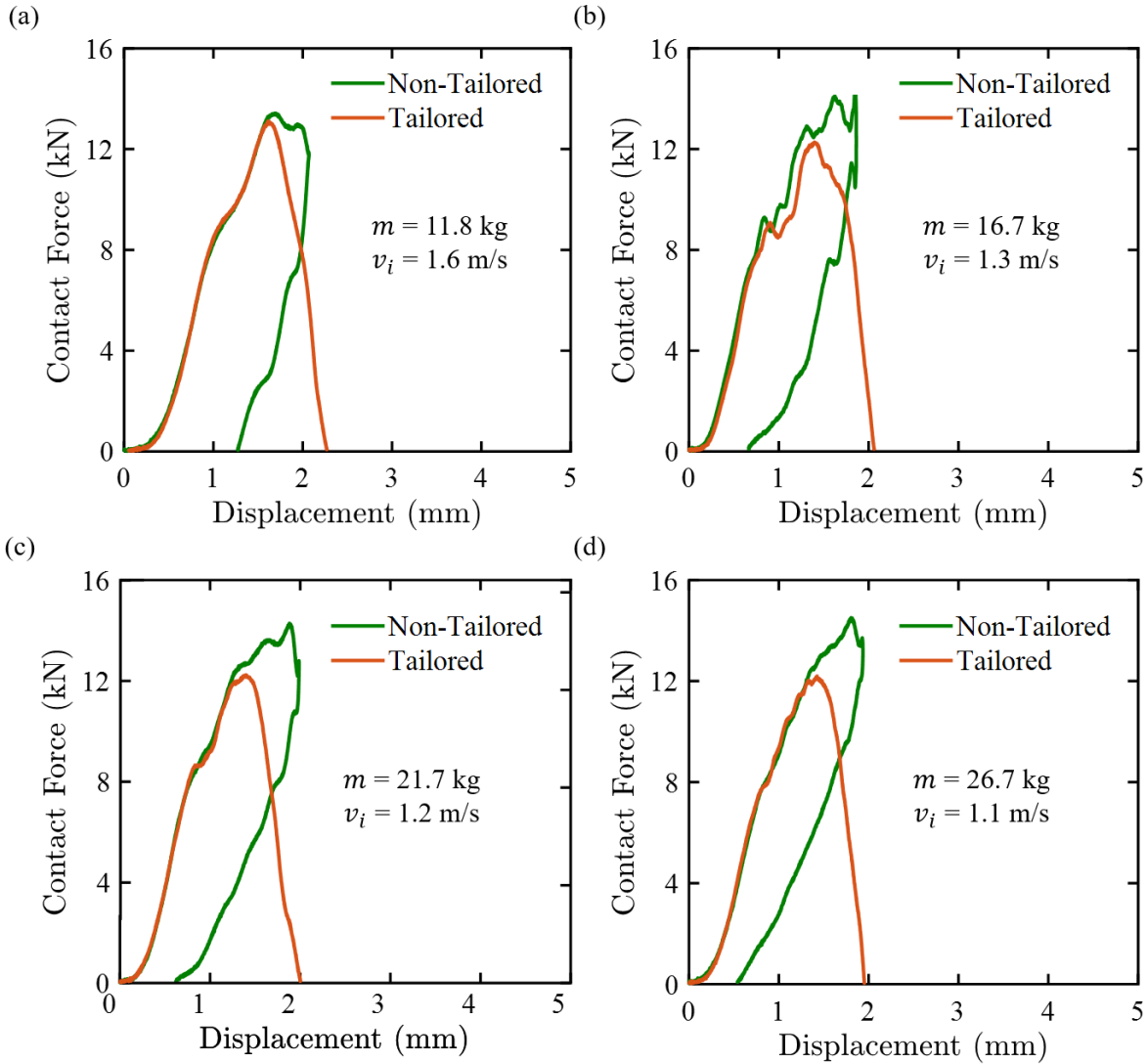


Figure 6: Contact force vs. displacement curves for geometrically tailored ( $\alpha = 0.4$  and  $\eta' = 0.7$ ) and non-tailored (i.e. uniform thickness,  $\alpha = 1.0$ ) honeycomb structures under equi-energetic impact at 15 J, realized with various combinations of impact mass and velocity: (a)  $m = 11.8$  kg,  $v_i = 1.6$  m/s, (b)  $m = 11.8$  kg,  $v_i = 1.3$  m/s, (c)  $m = 11.8$  kg,  $v_i = 1.2$  m/s, and (d)  $m = 11.8$  kg,  $v_i = 1.1$  m/s.

For both the tailored and non-tailored honeycombs, the observed increase in residual deformation (Fig. 7b) and absorbed energy (Fig. 7c) with increasing impact velocity can be attributed to viscoelastic

stiffening of the polymeric bulk material and the concomitant decrease in the material's yield/failure strain which, in turn, limits the elastic strain energy that can be stored in the sample. We also observe from Fig. 7c that the tailored honeycombs absorbed nearly the entire energy carried by the impactor (15 J) due to the occurrence of inelastic deformation and axial crushing of the cell walls, and only a very small portion of elastic energy was recovered upon unloading. Post-test photographs (see Fig. S5, Supplementary Material) show that the extent of impact damage in the tailored honeycomb increased with increasing impact velocity, which agrees with the measurements presented in Fig. 7b.

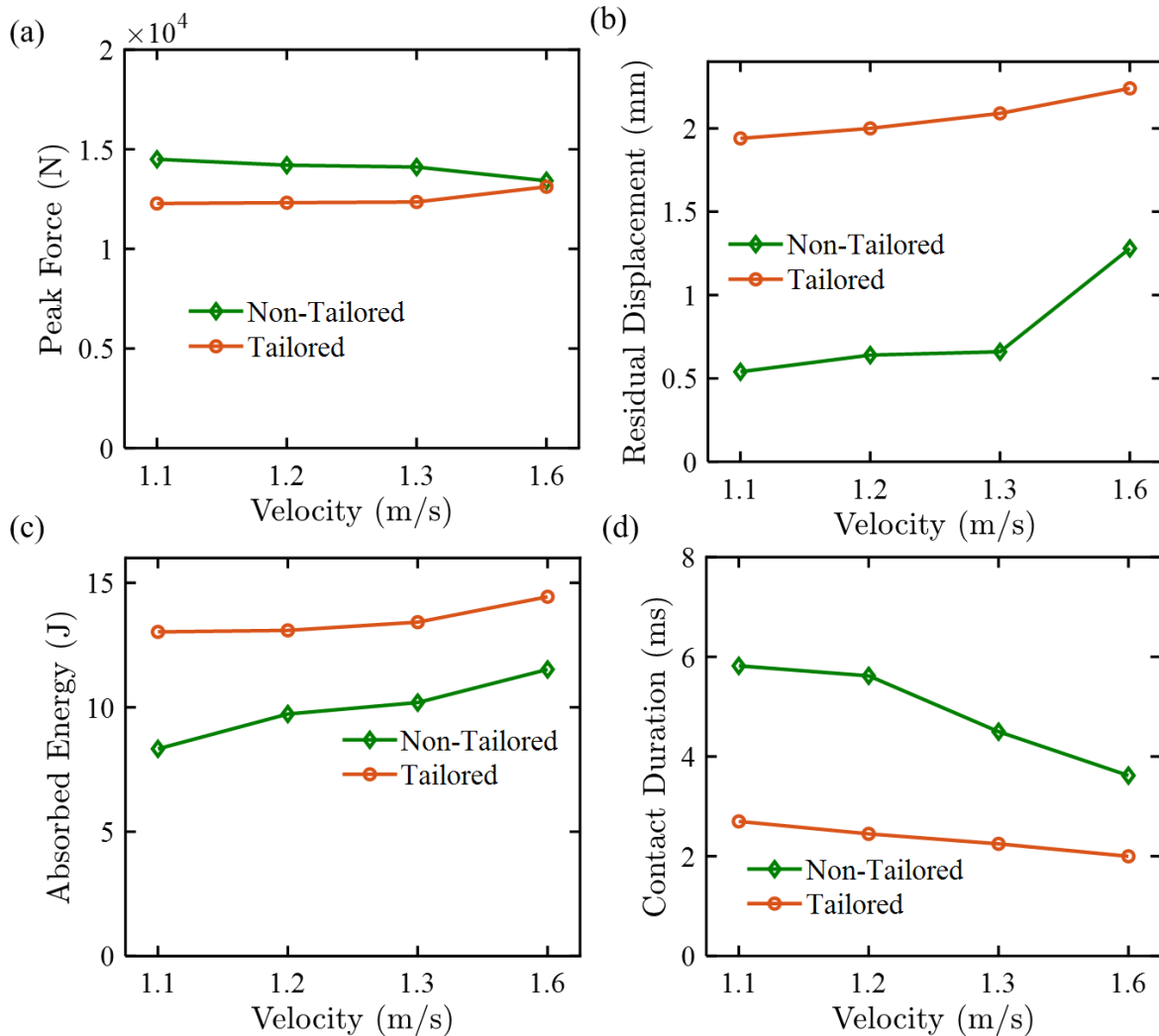


Figure 7: (a) Peak contact force, (b) residual displacement, (c) absorbed energy and (d) contact duration of geometrically tailored ( $\alpha = 0.4$  and  $\eta' = 0.7$ ) and non-tailored honeycombs obtained from equi-energetic impact tests at 15 J, realized with various combinations of impact mass  $m$  and velocity  $v_i$ .

Furthermore, we observe from Fig. 7d that, for both the non-tailored and tailored honeycombs, the total contact duration increases with decreasing impact velocity (or increasing drop weight). This is consistent with prior experimental work [63] and can be explained by the fact that the impact duration is controlled by the momentum of the impactor, which changes with increasing impact mass (or decreasing impact velocity) if the impact energy is kept fixed, as it is evident from Table 2. This has also been confirmed by FE calculations performed for equi-energetic impacts with a higher level of impact energy (125 J), as will be discussed next.

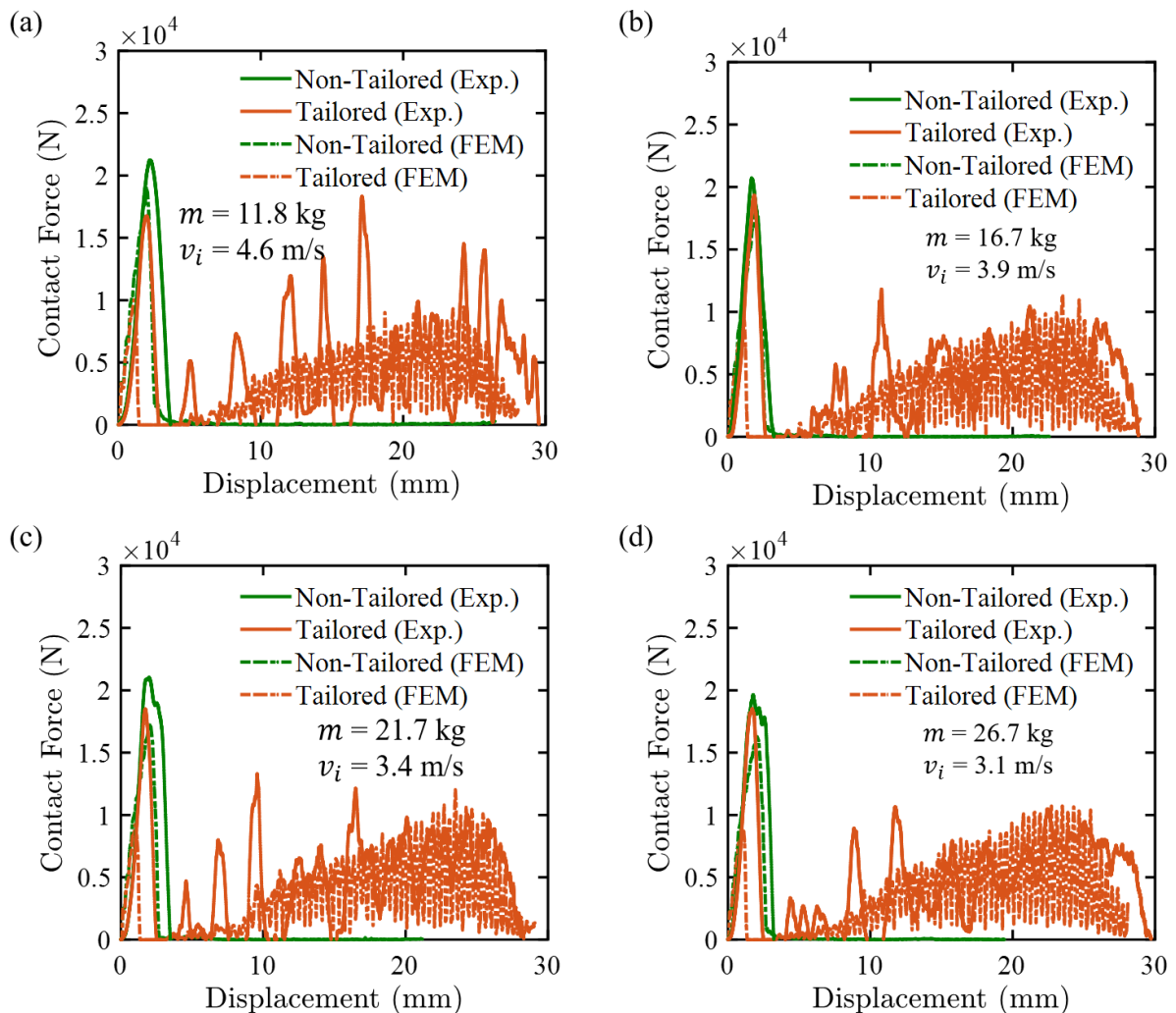


Figure 8: Comparison of FEM and experimental results: Contact force vs. displacement curves of geometrically tailored ( $\alpha = 0.4$  and  $\eta' = 0.7$ ) and non-tailored honeycombs under equi-energetic impact at 125 J, realized with various combinations of impact mass  $m$  and velocity  $v_i$ .

In Fig. 8, we present a comparison between the measured and predicted contact force vs. displacement profiles for equi-energetic impacts performed at an elevated impact energy of 125 J using the same drop weights as in the 15 J tests, but with increased impact velocity in the range  $3.1 \leq v_i \leq 4.6$  m/s. Note that the corresponding time histories of absorbed energy are plotted in Fig. S6 (Supplementary Material). Similar to what we observed from Fig. 2, the non-tailored samples collapse suddenly in the impact tests after reaching an initial peak force of  $\approx 20$  kN, while the tailored honeycomb ( $\alpha = 0.4$  and  $\eta' = 0.7$ ) exhibits signs of progressive damage and crushing evinced by an extended “fluctuating plateau” following the initial peak load (see Fig. 8). The FE calculations capture the observed trends with adequate accuracy, but somewhat under-predict the contact forces before and after the initial peak, which was also observed in Fig. 3 and discussed in Section 4.1. The corresponding post-test photographs (see Fig. S7, Supplementary Material) show that the non-tailored honeycombs were reduced to pools of fragments by the impacting striker, while the tapered base of the graded honeycombs remained partially intact, due to the progressive crushing of the tailored structure (see Fig. 4).

Furthermore, we deduced from Figs. 8 and S6 (Supplementary Material) the measured and predicted peak contact forces, crush length (i.e. the length over which the sample exerts a resisting force on the impactor), absorbed energies and contact durations and plotted the obtained data in Fig. 9 as functions of the impact velocity. The numerical values plotted in Fig. 9 are listed in Table S4 (Supplementary Material), for reference. Similar to what we observed from Fig. 7a for the 15 J case, the peak contact forces of the non-tailored samples in Fig. 9a are higher than those of the tailored ones for all impact velocities considered here. This is in qualitative agreement with the FE predictions, and can be attributed to the smaller neck thickness,  $t_{min}$ , in the tailored sample with  $\alpha = 0.4$  and  $\eta' = 0.7$  (see Table 1), resulting in a lower collapse stress. However, the presence of a tapered base in the tailored samples prevented the occurrence of sudden failure by global buckling (as illustrated in Fig. 4a) enabling a more stable collapse response and resulting in considerable increases in the crush length (see Fig. 9b) and absorbed energy (see Fig. 9c) which were found to be nearly insensitive to variations in the impact speed for the conditions considered here.

While these trends are well captured by the FE calculations, the predicted values of absorbed energy lie well below the measurements in Fig. 9c which is a direct consequence of the lower collapse strength predicted by the FE models, as seen from Fig. 9a. Similar to what has been reported in Fig. 7 for the 15 J impacts, increasing the impact velocity at a constant energy of 125 J decreases the duration of the impact event which is evident from the predictions and measurements in Fig. 9d, showing a steady reduction in contact time with increasing impact velocity.

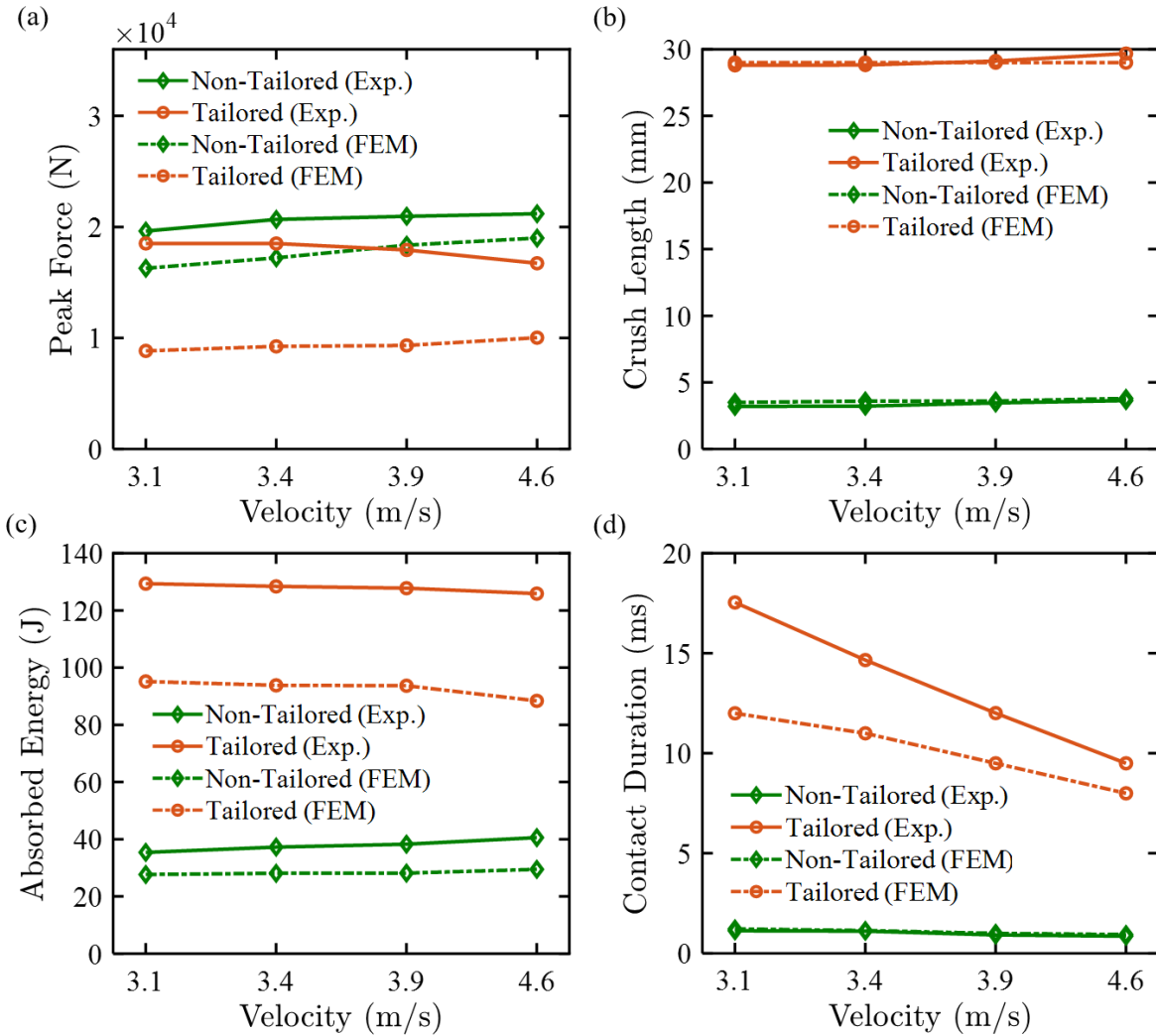


Figure 9: Comparison of FEM and experimental results: (a) peak contact force, (b) crush length, (c) absorbed energy and (d) contact duration of geometrically tailored ( $\alpha = 0.4$  and  $\eta' = 0.7$ ) and non-tailored honeycombs obtained from equi-energetic impact tests at 125 J, realized with various combinations of impact mass  $m$  and velocity  $v_i$ .

Based on these data presented in this section, it can be concluded that the geometrical tailoring scheme, proposed here, can substantially enhance the impact performance of a honeycomb structure when the impact is severe (i.e. 125 J in this study), but can also lead to increased structural damage at relatively low levels of impact energy (i.e. 15 J in this study). In a previous study [7], we showed that the same non-tailored honeycomb as considered herein remained widely undamaged for impact energies  $< 55$  J, but collapsed suddenly by the propagation of unstable cracks (as observed here) when the impact energy was raised beyond 55 J, resulting in a limited energy absorption ( $< 50$  J) even at impact energies as high as 130 J. Hence, for the honeycomb structures used in this study, the geometrical tailoring scheme can be considered beneficial in terms of impact performance, if the the impact energy is around 55 J and above.

### **3.3. Impact response of honeycombs with periodic thickness variations in the out-of-plane direction**

The bilinear wall thickness tailoring strategy of honeycombs examined in the previous sections can be extended to create graded honeycombs with periodic variations in wall thickness in the out-of-plane direction. To explore this further, we use the following notation to describe the nature of the periodic gradation pattern,  $[\alpha, \eta']_{ns}$  where  $n$  is the number of bilinear gradation patterns in the out-of-plane direction with identical design parameters  $\alpha$  and  $\eta'$ , and  $s$  is an optional index indicating the symmetric nature of the stack about the mid-plane (then  $n$  is the number of gradation patterns in the bottom half of the stack only). We now consider a symmetric stack of two bilinear gradation patterns with identical normalized gradation length  $\eta' = 1$  and equal but opposite gradation parameter  $\alpha = \mp 0.4$ , giving a stacking sequence of either  $[0.4, 1.0]_{1s}$  or  $[-0.4, 1.0]_{1s}$ , as shown in Fig. 10a. We keep the overall dimensions of the (stacked) samples as before ( $41.4 \text{ mm} \times 41.4 \text{ mm} \times 30 \text{ mm}$ ) and set  $t_{\max} = 1.43 \text{ mm}$  and  $t_{\min} = 0.57 \text{ mm}$  to obtain the same weight as the samples listed in Table 1.

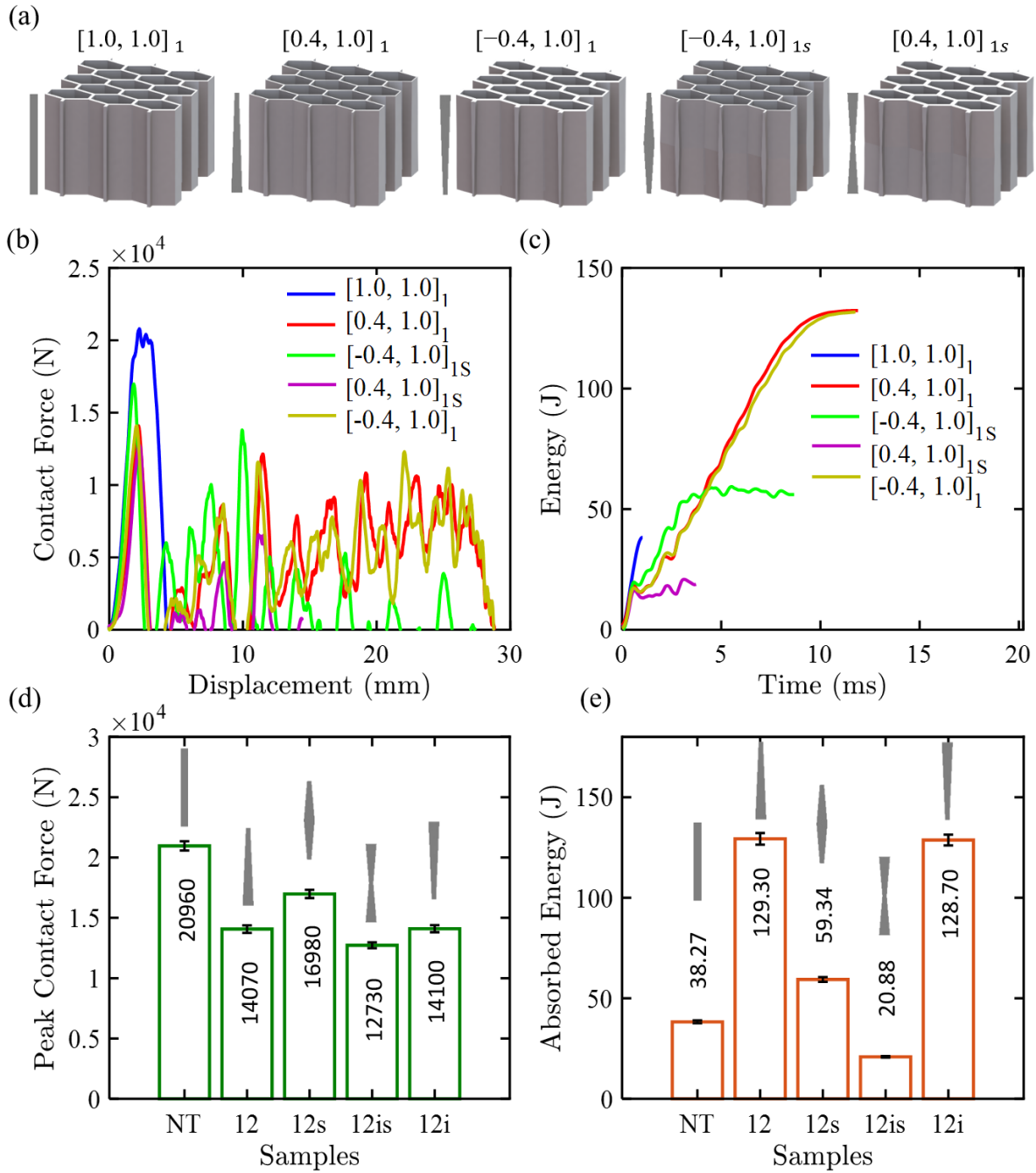


Figure 10: (a) CAD images of honeycombs with uniform thickness  $[1.0, 1.0]$ , bilinear gradation patterns,  $[0.4, 1.0]_1$  and  $[-0.4, 1.0]_1$ , respectively, and periodic gradation patterns,  $[-0.4, 1.0]_{1s}$  and  $[0.4, 1.0]_{1s}$ , respectively; (b) contact force vs. displacement curves, (c) absorbed energy vs. time histories, (d) peak contact force and (e) total absorbed energy for the honeycomb structures shown in (a) subject to low-velocity impact at 130 J.

We now compare the impact responses of the honeycombs with periodically varying wall thickness in the out-of-plane direction  $[0.4,1.0]_{1s}$  and  $[-0.4,1.0]_{1s}$  to those of their non-stacked counterparts which are denoted here as  $[0.4,1.0]_1$  and  $[-0.4,1.0]_1$  for consistency. Note that sample  $[0.4,1.0]_1$  is identical to sample 12 in Table 1 and  $[-0.4,1.0]_1$  is the inverted version of that sample (see Fig. 10a). In Fig. 10b, we plot the contact force vs. displacement curves of honeycombs with bilinear and periodic gradation patterns subject to an impact energy of 130 J ( $m = 16.75$  kg,  $v_i = 3.86$  m/s), while the corresponding time histories of the absorbed energies are presented in Fig. 10c; for comparison, we also include the measurements obtained for the non-tailored sample of equal mass  $[1.0,1.0]_1$ .

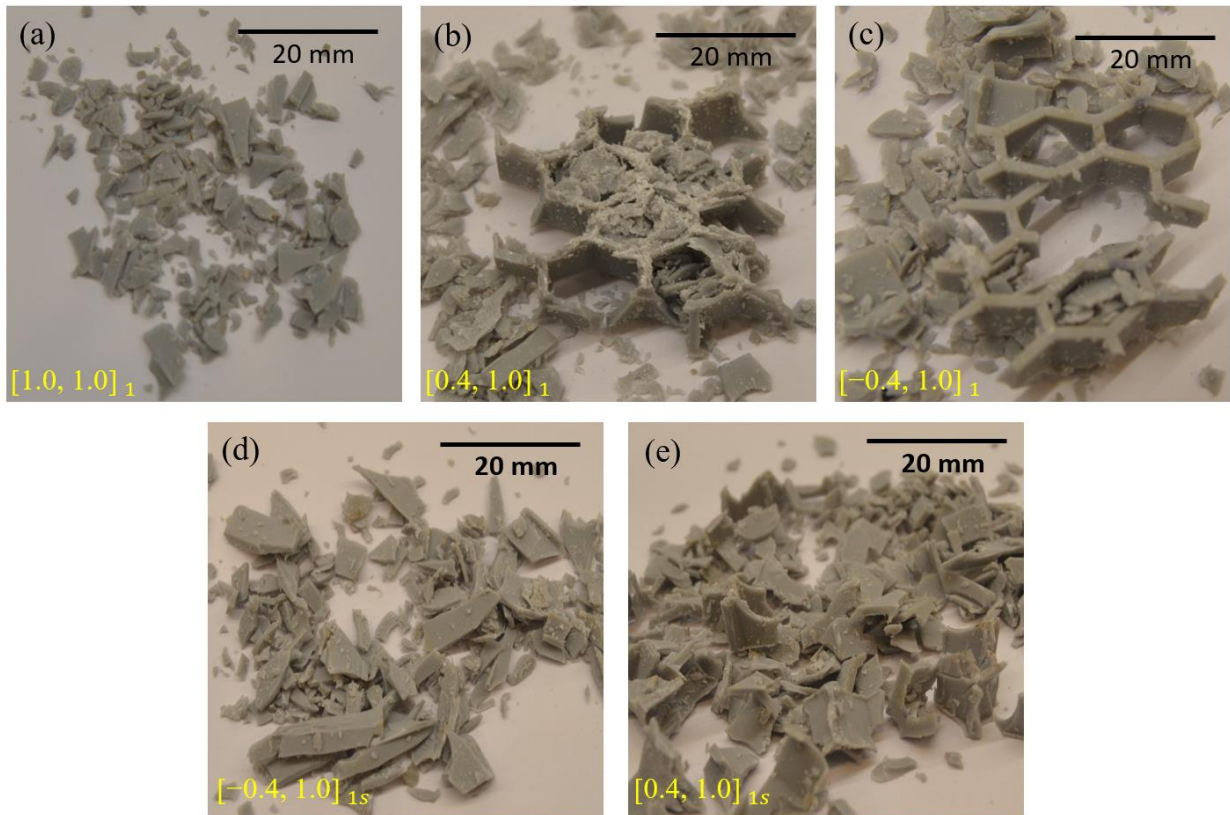


Figure 11: Post-test photographs of honeycomb structures subject to low-velocity impact at 130 J: (a) honeycombs with uniform thickness  $[1.0,1.0]$ , (b-c) bilinearly graded honeycombs,  $[0.4,1.0]_1$  and  $[-0.4,1.0]_1$ , respectively, and (d-e) periodically wall thickness graded honeycombs,  $[-0.4,1.0]_{1s}$  and  $[0.4,1.0]_{1s}$ , respectively.

As seen from Fig. 10b, the impact force induced in the non-tailored sample drops rapidly after reaching a peak, and the corresponding energy vs. time curve rises nearly linearly up to 49.1 J (see Fig. 10c) before the sample collapses rapidly. On the other hand, the contact force vs. displacement curves of all geometrically tailored honeycombs show multiple fluctuations following the initial peak, indicating a more stable collapse response induced by multiple progressive brittle fractures of the cell walls during compression [64]. Accordingly, the energy vs. time histories of the graded honeycombs show an initial linear regime, associated with the first peak in the force-displacement response, followed by a fluctuating regime, in which the absorbed energy rises steadily over an extended period of time. While the highest peak contact force was recorded for the non-tailored sample, no distinct trends can be observed among the tailored honeycombs (see Fig. 10d). However, the total energies absorbed by the honeycombs with bilinear gradients,  $[-0.4,1.0]_1$  and  $[0.4,1.0]_1$ , respectively, by far exceed those of their periodically tailored counterparts,  $[-0.4,1.0]_{1s}$  and  $[0.4,1.0]_{1s}$ , respectively, as seen from Fig. 10e.

We note that the periodically tailored honeycomb with  $[0.4,1.0]_{1s}$  absorbed less energy than the non-tailored  $[1.0,1.0]_1$ , suggesting that the existence of a neck in the mid-plane of the honeycomb can trigger unstable collapse modes upon the impact. This also highlights that the use of periodically varying geometric gradation patterns in honeycombs can lead to inferior impact performance under out-of-plane compression and should therefore not be arbitrarily chosen.

The corresponding post-test photographs illustrated in Fig. 11, show that the honeycombs with the lowest energy absorption (i.e. the  $[0.4,1.0]_{1s}$  and  $[1.0,1.0]_1$ ) disintegrated completely upon the impact and only scattered fragments remained, corroborating the hypothesis that these samples collapsed in a brittle manner. In contrast, the wide base of the bilinearly graded  $[0.4,1.0]_1$  honeycomb remained partly intact after the impact (see Fig. 11b), which suggests that the collapse process initiated at the top face where the cell walls are thin, and then advanced in a progressive manner towards the bottom face. Similar observations are made for the (inverted)  $[-0.4,1.0]_1$  honeycomb (see Fig. 11c), where the intact portion of the honeycomb is found on top of a pile of fragments, indicating that the sample collapsed progressively from the bottom

to the top, as expected. Based on the observations and measurements presented in this section, we conclude that the honeycombs with bilinearly graded walls in the out-of-plane direction show superior out-of-plane impact performance over their periodically tailored and non-tailored counterparts and should therefore be highly useful for versatile application in impact and blast protection.

## 4. Conclusions

In this paper, we experimentally and numerically examined the energy absorption characteristics and damage mechanisms of geometrically tailored honeycombs subject to low-velocity impact in the through-thickness direction. With the aim to mitigate sudden collapse by global buckling of the cell walls, we proposed a novel tailoring strategy which bilinearly grades the wall thickness of the honeycombs in the out-of-plane direction. The tailoring strategy proposed has two design parameters, namely, the gradation parameter  $\alpha$  and the normalized gradation length  $\eta'$ . Based on the proposed scheme, hexagonal honeycombs with varying design parameters  $[\alpha, \eta']$  and equal mass were designed, and 3D printed via the DLP additive manufacturing. Low-velocity impact tests and dynamic FE calculations were performed to examine the collapse response of the geometrically tailored honeycombs and compare their energy absorption characteristics and collapse mechanisms to those observed in conventional (non-tailored) honeycombs of the same mass. In addition, equi-energetic impact tests were performed on selected honeycomb designs to examine the effects of impact mass and velocity on their dynamic collapse response at both low (15 J) and high levels (130 J) of impact energy. We also examined the effect of impact direction by inverting the gradation pattern in the honeycomb structure and explored the impact responses of honeycombs with periodic variations in the cell-wall thickness, obtained by stacking bilinear gradation patterns in a systematic manner.

At low levels of impact energy (15 J), the deformation in the non-tailored honeycomb was predominantly elastic and no signs of damage were found in the specimens following the impact. In contrast, the geometrically tailored honeycomb with  $\alpha = 0.4$  and  $\eta' = 0.7$ , partially collapsed under the same conditions, showing that the bilinear gradation pattern can reduce the ultimate load capacity of the

honeycomb structure at low impact loads. At higher levels of impact energy, however, it was found that the bilinearly wall-thickness tailored honeycombs consistently outperformed their non-tailored counterparts (130 J) in terms of impact performance, reporting an increase in energy absorption of about 250 %. Such remarkable enhancement in energy absorption was attributed to a transition in the underlying collapse mechanism from global buckling of the honeycomb structure to progressive crushing of the cell walls, which was observed from high-speed images and dynamic FE calculations. With a careful selection of design parameters  $[\alpha, \eta']$ , we demonstrated experimentally that it is practically possible to achieve simultaneous increases in energy absorption and impact resistance as compared to the non-tailored honeycombs. The results obtained from equi-energetic impacts at 130 J showed that the energies absorbed by the geometrically tailored honeycombs were nearly insensitive to variations in impact mass and speed for nominal strain rates ranging over  $4.3 \leq \dot{\epsilon} \leq 6.4 \text{ s}^{-1}$ . Our measurements also revealed that the impact responses of geometrically tailored honeycombs with inverted gradation patterns are very similar to those of their non-inverted counterparts, concluding that the latter honeycombs are effective energy absorbers regardless of whether the impact occurs on the top or bottom face. We also observed that architected honeycombs with periodically varying wall thickness, collapsed rapidly upon the impact of the drop weight, leading to reduced energy absorption capacity as compared to those with bilinear gradation patterns. This suggests that honeycombs with periodically varying wall-thickness in the out-of-plane direction may not yield advantaged energy absorption performance and can therefore be disregarded in the design of impact and blast-resistant structures.

We have further demonstrated that the bilinearly wall-thickness graded honeycombs, realized via additive manufacturing, offer the possibility of tuning impact resistance and energy absorption to specific requirements and should therefore be suitable for versatile application in impact and blast protection. It is recommended to direct future research efforts towards the identification of optimal design parameters that maximize the energy absorption and/or collapse strength of a honeycomb structure, an aspect that has not been addressed in this study. Finally, it is worth mentioning that the proposed tailoring scheme is generic

and can therefore be applied to other types of cellular structures, such as strut-based lattices, where gradients in the strut thickness could be employed to enhance energy absorption and impact resistance by controlling the collapse mode of the structure. It is therefore anticipated that the findings of this study will stimulate further research into the design of cellular material architectures that provide optimal protection against impact and blast.

## Acknowledgments

SK would like to thank the University of Glasgow for the start-up grant [award no: 144690-01]. JS acknowledges EPSRC DTA PhD studentship [Award No: EP/R513222/1]. Authors would like to thank the Abu Dhabi National Oil Company (ADNOC) for providing the research grant [grant number: EX2016-000010]. This work was partially funded by Khalifa University through the Competitive Internal Research Award [grant number: CIRA-2018-128] and the Abu Dhabi Department of Education of Knowledge (ADEK) through the Award for Research Excellence (AARE) 2019 [grant number: AARE19-148].

## References

1. Sun, G., et al., *Crashworthiness optimization of automotive parts with tailor rolled blank*. Engineering Structures, 2018. **169**: p. 201-215.
2. Abramowicz, W., *Thin-walled structures as impact energy absorbers*. Thin-Walled Structures, 2003. **41**(2): p. 91-107.
3. Sun, G., et al., *Crashing analysis and multiobjective optimization for thin-walled structures with functionally graded thickness*. International Journal of Impact Engineering, 2014. **64**: p. 62-74.
4. Andrew, J.J., et al., *Energy absorption and self-sensing performance of 3D printed CF/PEEK cellular composites*. Materials & Design, 2021. **208**: p. 109863.
5. Sun, G., et al., *Energy absorption mechanics for variable thickness thin-walled structures*. Thin-Walled Structures, 2017. **118**: p. 214-228.
6. Mousanezhad, D., et al., *Impact resistance and energy absorption of regular and functionally graded hexagonal honeycombs with cell wall material strain hardening*. International Journal of Mechanical Sciences, 2014. **89**: p. 413-422.
7. Andrew, J.J., et al., *Impact performance enhancement of honeycombs through additive manufacturing-enabled geometrical tailoring*. International Journal of Impact Engineering, 2019. **134**: p. 103360.
8. Xu, M., et al., *Mechanical properties and energy absorption capability of AuxHex structure under in-plane compression: Theoretical and experimental studies*. International Journal of Mechanical Sciences, 2019. **159**: p. 43-57.

9. Weidmann, J., A. Großmann, and C. Mittelstedt, *Laser powder bed fusion manufacturing of aluminum honeycomb structures: Theory and testing*. International Journal of Mechanical Sciences, 2020. **180**: p. 105639.
10. Gao, Q., W.-H. Liao, and L. Wang, *An analytical model of cylindrical double-arrowed honeycomb with negative Poisson's ratio*. International Journal of Mechanical Sciences, 2020. **173**: p. 105400.
11. Mahbod, M. and M. Asgari, *Elastic and plastic characterization of a new developed additively manufactured functionally graded porous lattice structure: Analytical and numerical models*. International Journal of Mechanical Sciences, 2019. **155**: p. 248-266.
12. Zhang, X. and H. Zhang, *Energy absorption of multi-cell stub columns under axial compression*. Thin-Walled Structures, 2013. **68**: p. 156-163.
13. Liu, Y. and X.-C. Zhang, *The influence of cell micro-topology on the in-plane dynamic crushing of honeycombs*. International Journal of Impact Engineering, 2009. **36**(1): p. 98-109.
14. Zhang, X. and H. Zhang, *Theoretical and numerical investigation on the crush resistance of rhombic and kagome honeycombs*. Composite Structures, 2013. **96**: p. 143-152.
15. Al Galib, D. and A. Limam, *Experimental and numerical investigation of static and dynamic axial crushing of circular aluminum tubes*. Thin-Walled Structures, 2004. **42**(8): p. 1103-1137.
16. Liu, L., H. Wang, and Z. Guan, *Experimental and numerical study on the mechanical response of Nomex honeycomb core under transverse loading*. Composite Structures, 2015. **121**: p. 304-314.
17. Alavi Nia, A. and M. Parsapour, *Comparative analysis of energy absorption capacity of simple and multi-cell thin-walled tubes with triangular, square, hexagonal and octagonal sections*. Thin-Walled Structures, 2014. **74**: p. 155-165.
18. Nian, Y., et al., *Crashworthiness design of self-similar graded honeycomb-filled composite circular structures*. Construction and Building Materials, 2020. **233**: p. 117344.
19. Sun, Z.P., Y.B. Guo, and V.P.W. Shim, *Characterisation and modeling of additively-manufactured polymeric hybrid lattice structures for energy absorption*. International Journal of Mechanical Sciences, 2021. **191**: p. 106101.
20. Ali, M., et al., *Theoretical and finite element study of a compact energy absorber*. Advances in Engineering Software, 2008. **39**(2): p. 95-106.
21. Ajdari, A., H. Nayeb-Hashemi, and A. Vaziri, *Dynamic crushing and energy absorption of regular, irregular and functionally graded cellular structures*. International Journal of Solids and Structures, 2011. **48**(3-4): p. 506-516.
22. Zhang, J., Z. Wang, and L. Zhao, *Dynamic response of functionally graded cellular materials based on the Voronoi model*. Composites Part B: Engineering, 2016. **85**: p. 176-187.
23. Wang, X., Z. Zheng, and J. Yu, *Crashworthiness design of density-graded cellular metals*. Theoretical and Applied Mechanics Letters, 2013. **3**(3): p. 031001.
24. Zheng, J., Q. Qin, and T. Wang, *Impact plastic crushing and design of density-graded cellular materials*. Mechanics of Materials, 2016. **94**: p. 66-78.
25. Shen, C., G. Lu, and T. Yu, *Dynamic behavior of graded honeycombs—a finite element study*. Composite structures, 2013. **98**: p. 282-293.
26. Shen, C.J., T. Yu, and G. Lu, *Double shock mode in graded cellular rod under impact*. International Journal of Solids and Structures, 2013. **50**: p. 217-233.
27. Wu, Y., et al., *Energy absorption of additively manufactured functionally bi-graded thickness honeycombs subjected to axial loads*. Thin-Walled Structures, 2021. **164**: p. 107810.
28. Wu, H., X. Zhang, and Y. Liu, *In-plane crushing behavior of density graded cross-circular honeycombs with zero Poisson's ratio*. Thin-Walled Structures, 2020. **151**: p. 106767.
29. Sun, G., et al., *An experimental and numerical study on quasi-static and dynamic crushing behaviors for tailor rolled blank (TRB) structures*. Materials & Design, 2017. **118**: p. 175-197.

30. Liu, H., et al., *Axial compression deformability and energy absorption of hierarchical thermoplastic composite honeycomb graded structures*. *Composite Structures*, 2020. **254**: p. 112851.
31. Feng, G., et al., *Energy absorption performance of honeycombs with curved cell walls under quasi-static compression*. *International Journal of Mechanical Sciences*, 2021. **210**: p. 106746.
32. Qi, D., et al., *Impact energy absorption of functionally graded chiral honeycomb structures*. *Extreme Mechanics Letters*, 2019. **32**: p. 100568.
33. Sun, G., et al., *On energy absorption of functionally graded tubes under transverse loading*. *International Journal of Mechanical Sciences*, 2016. **115-116**: p. 465-480.
34. Alia, R.A., et al., *The energy-absorbing characteristics of carbon fiber-reinforced epoxy honeycomb structures*. *Journal of Composite Materials*, 2018. **53**(9): p. 1145-1157.
35. Wei, Y., et al., *Effects of different configurations and gradients on compression responses of gradient honeycombs via selective laser melting*. *Thin-Walled Structures*, 2022. **170**: p. 108462.
36. Liu, H., E.T. Zhang, and B.F. Ng, *In-plane dynamic crushing of a novel honeycomb with functionally graded fractal self-similarity*. *Composite Structures*, 2021. **270**: p. 114106.
37. Fang, J., et al., *On hierarchical honeycombs under out-of-plane crushing*. *International Journal of Solids and Structures*, 2018. **135**: p. 1-13.
38. Zhang, X., Z. Wen, and H. Zhang, *Axial crushing and optimal design of square tubes with graded thickness*. *Thin-Walled Structures*, 2014. **84**: p. 263-274.
39. Zhao, L. and W.Q. Chen, *Symplectic analysis of plane problems of functionally graded piezoelectric materials*. *Mechanics of Materials*, 2009. **41**(12): p. 1330-1339.
40. Fang, J., et al., *Dynamic crashing behavior of new extrudable multi-cell tubes with a functionally graded thickness*. *International Journal of Mechanical Sciences*, 2015. **103**: p. 63-73.
41. Xu, F., *Enhancing material efficiency of energy absorbers through graded thickness structures*. *Thin-Walled Structures*, 2015. **97**: p. 250-265.
42. Logakannan, K.P., et al., *Mechanical response of a novel hybrid tube composed of an auxetic outer layer*. *Thin-Walled Structures*, 2022. **171**: p. 108649.
43. Chen, G., et al., *Blast resistance of metallic double arrowhead honeycomb sandwich panels with different core configurations under the paper tube-guided air blast loading*. *International Journal of Mechanical Sciences*, 2021. **201**: p. 106457.
44. Zhou, Y., L. Ye, and W. Chen, *Impact mitigation performance of hybrid metamaterial with a low frequency bandgap*. *International Journal of Mechanical Sciences*, 2022. **213**: p. 106863.
45. Adams, R., et al., *Mechanical behaviour of additively manufactured elastomeric pre-buckled honeycombs under quasi-static and impact loading*. *Materials & Design*, 2022. **213**: p. 110368.
46. Meng, Y., et al., *Study on the dynamic response of combined honeycomb structure under blast loading*. *Thin-Walled Structures*, 2020. **157**: p. 107082.
47. Kholoosi, F. and S.A. Galehdari, *Design and Analysis of a Helmet Equipped with Graded Honeycomb Structure Under Impact of Flat and Hemi-spherical Anvils*. *Procedia Engineering*, 2017. **173**: p. 1299-1306.
48. Tan, H.L., et al., *Energy absorption characteristics of three-layered sandwich panels with graded re-entrant hierarchical honeycombs cores*. *Aerospace Science and Technology*, 2020. **106**: p. 106073.
49. Ubaid, J., B.L. Wardle, and S. Kumar, *Bioinspired Compliance Grading Motif of Mortar in Nacreous Materials*. *ACS Applied Materials & Interfaces*, 2020. **12**(29): p. 33256-33266.
50. Ubaid, J., B.L. Wardle, and S. Kumar, *Strength and Performance Enhancement of Multilayers by Spatial Tailoring of Adherend Compliance and Morphology via Multimaterial Jetting Additive Manufacturing*. *Scientific Reports*, 2018. **8**(1): p. 13592.

51. Kumar, S., B.L. Wardle, and M.F. Arif, *Strength and Performance Enhancement of Bonded Joints by Spatial Tailoring of Adhesive Compliance via 3D Printing*. ACS Applied Materials & Interfaces, 2017. **9**(1): p. 884-891.
52. Zhang, Y., et al., *Dynamic compressive response of additively manufactured AlSi10Mg alloy hierarchical honeycomb structures*. Composite Structures, 2018. **195**: p. 45-59.
53. Kumar, S., et al., *Tunable energy absorption characteristics of architected honeycombs enabled via additive manufacturing*. ACS applied materials & interfaces, 2019. **11**(45): p. 42549-42560.
54. Wang, Z., et al., *Compression behavior of strut-reinforced hierarchical lattice—Experiment and simulation*. International Journal of Mechanical Sciences, 2021. **210**: p. 106749.
55. Andrew, J.J., P. Verma, and S. Kumar, *Impact behavior of nanoengineered, 3D printed plate-lattices*. Materials & Design, 2021. **202**: p. 109516.
56. Andrew, J.J., et al., *Energy absorption characteristics of additively manufactured plate-lattices under low- velocity impact loading*. International Journal of Impact Engineering, 2021. **149**: p. 103768.
57. Alam, F., K.M. Varadarajan, and S. Kumar, *3D printed polylactic acid nanocomposite scaffolds for tissue engineering applications*. Polymer Testing, 2020. **81**: p. 106203.
58. Mueller, J. and K. Shea, *Stepwise graded struts for maximizing energy absorption in lattices*. Extreme Mechanics Letters, 2018. **25**: p. 7-15.
59. Drucker, D.C. and W. Prager, *SOIL MECHANICS AND PLASTIC ANALYSIS OR LIMIT DESIGN*. Quarterly of Applied Mathematics, 1952. **10**(2): p. 157-165.
60. Kontou, E., *Viscoplastic deformation of an epoxy resin at elevated temperatures*. Journal of Applied Polymer Science, 2006. **101**: p. 2027-2033.
61. Mayr, A., W. Cook, and G. Edward, *Yielding behaviour in model epoxy thermosets - I. Effect of strain rate and composition*. Polymer, 1998. **39**: p. 3719-3724.
62. Buckley, C., et al., *Deformation of thermosetting resins at impact rates of strain. Part I: Experimental study*. Journal of the Mechanics and Physics of Solids, 2001. **49**: p. 1517-1538.
63. Lee, S., et al., *Deformation rate effects on failure modes of open-cell Al foams and textile cellular materials*. International Journal of Solids and Structures - INT J SOLIDS STRUCT, 2005. **43**.
64. Zhai, J., et al., *Energy absorption of pre-folded honeycomb under in-plane dynamic loading*. Thin-Walled Structures, 2019. **145**: p. 106356.